Van der Pol–Duffing oscillator and its application to gain-driven light-matter interaction

Chunlei Zhang,[1,†] Mun Kim,[1,†] Jianbo Wang,[2] and Can-Ming Hu[1,*]

[1] *Department of Physics and Astronomy, University of Manitoba, Winnipeg, Manitoba R3T 2N2, Canada*

[2] *School of Physical Science and Technology, Lanzhou University, Lanzhou, 730000, People's Republic of China*

(Received 18 March 2024; revised 15 May 2024; accepted 17 June 2024; published 15 July 2024)

We report the observation of frequency nonlinearity within a gain-embedded resonator. A coupling model, integrating the van der Pol–Duffing oscillator, is theoretically proposed. The proposed model is substantiated through experimental verification in coupled *LRC* circuits, demonstrating bistable behavior. Furthermore, by application of the van der Pol–Duffing oscillator to a gain-embedded microwave cavity, our model is demonstrated as an alternative theoretical perspective for understanding the gain-driven polariton.

DOI: 10.1103/PhysRevApplied.22.014034

I. INTRODUCTION

In systems with inherent frequencies, self-oscillation manifests itself as an amplification of magnitude culminating in a stable state, without reliance on external forces. The phenomenon can be effectively modeled by one introducing a negative resistance into an *LRC* circuit, a concept originally formulated by van der Pol [1]. Recognized as a classical model—van der Pol (vdP) oscillator in the academic literature—it forms a foundational element in the study of chaotic systems [2,3]. Beyond its engineering roots, the model exhibits profound versatility across various fields. The model offers insightful perspectives on phenomena such as the output of semiconductor laser diodes [4]. It is also extended to explore synchronization phenomena in the quantum field [5,6]. In the realm of biology, the vdP oscillator provides insights into the rhythmic dynamics of various biological processes, including cardiac cycles [7], neuronal activities [8], circadian rhythms [9], and human thermoregulatory mechanisms [10].

Besides the vdP oscillator, the Duffing oscillator is also a canonical nonlinear model. The latter characterizes the frequency as a variable dependent on amplitude [2,11], recognized as the Kerr nonlinearity [12,13]. Experimentally, the Kerr nonlinearity can be observed in nonlinear systems, such as cavity-magnonic systems [14,15], with the high-power external driving force, and it is commonly manifested as a frequency shift depending on the driving power.

The vdP oscillator and the Duffing oscillator are traditionally viewed as distinct physical models. Nonetheless, Shinriki *et al.* [16] first introduced the van der Pol–Duffing (vdP-D) oscillator, a model accounting for oscillations with both nonlinear damping and frequency. The vdP-D oscillator has been predominantly analyzed within the context of strong nonlinearity, particularly in chaos theory [17–21]. Our investigation extends the application of the vdP-D oscillator to coupled systems. Since the relative phase and the amplitude ratio between coupled oscillators are hard to measure in the light-matter system, the coupled dynamics, characterized by the bistability, is first theoretically studied and then experimentally manifested within a coupled-*LRC*-circuit model.

We apply this model to a cavity-magnonic system [22–26], where microwave cavity photons couple with spin excitations of a yttrium iron garnet (YIG) sphere. By our incorporating a microwave gain block into this system, it facilitates a steady state of the polariton, achieved while the supplied gain surpasses the polaritons' effective linear loss [27]. The bistable phenomenon is observed in this gain-loss system. In contrast to previous studies where the bistability of gain-driven polaritons was attributed to the dissipative coupling [27], our experimental exploration introduces an alternative pathway to bistability via a Kerr nonlinearity of the vdP-D oscillator.

II. THEORY

In Fig. 1(a), a gain-embedded *LC* circuit $\omega_1 = 1/\sqrt{LC}$ and its voltage oscillation are shown. Traditionally, the gain block's nonlinearity is assumed to manifest itself solely as a nonlinear resistance. If we define this oscillation as $V(t) = \frac{1}{2}[a(t)e^{i\omega_1 t} + \text{c.c.}]$, under weak nonlinearity, the amplitude of a vdP oscillator can be written in the

*Contact author: hu@physics.umanitoba.ca

†These authors contributed equally to this work.

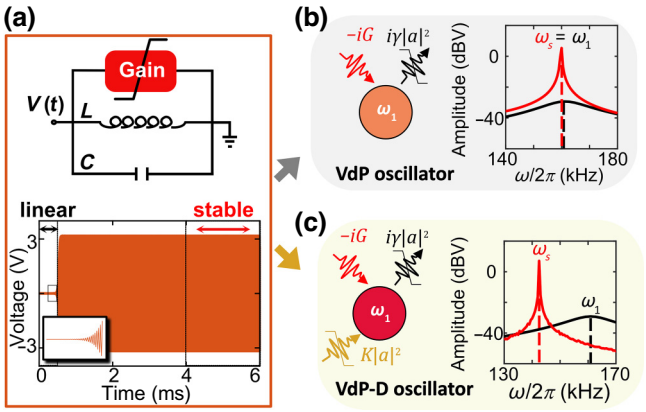

FIG. 1. (a) Gain-embedded LC resonator $\omega_1/2\pi = 159.40$ kHz, along with a schematic of its voltage dynamics. Given an initial voltage of 1 pV, the linear state is defined as the voltage oscillation below 1.1 V, while the stable state is defined as oscillations between 4 and 6 ms. (b),(c) vdP and vdP-D oscillators, featuring the frequency discrepancy between two states, where $G/2\pi = 7.74$ kHz, $\gamma/2\pi = 0.78$ kHz/V^2, and $K/2\pi = 1.59$ kHz/V^2. The spectra were obtained by Fourier transform.

form [2]

$$\frac{da}{dt} = (G - \gamma|a|^2)a, \tag{1}$$

where G is the effective gain factor and γ is the nonlinear-damping factor. Using amplitude as the distinguishing criterion, we can categorize the circuit's behavior into two states: "linear" and "stable." According to Eq. (1), in the small-amplitude regime, the nonlinear-damping term is negligible, rendering the system akin to a linear oscillator as shown in the inset in the voltage oscillation. As the amplitude increases to a constant $|a_0| = \sqrt{G/\gamma}$, where the gain is counteracted by the nonlinear damping, the system enters the stable state.

Our study starts from the frequencies of "linear" and "stable" states, where the stable state corresponds to the limit cycle of the oscillator. As shown in Fig. 1(b), the gain-embedded oscillator, schematized as a vdP oscillator with gain and nonlinear damping, always operates at a constant frequency for both the linear state and the stable state, denoted as $\omega_1 = \omega_s$. However, such a model primarily holds true for passive systems under small-signal conditions [28]. In the active system, characterized by large-amplitude oscillations, the system's reactance will become amplitude dependent [28], leading to a dependency of the frequency on the amplitude. So, Kerr nonlinearity is necessary to account for the frequency shift between the stable state and the linear state. Then, the modified model, termed the "vdP-D oscillator," is formulated as follows:

$$\frac{da}{dt} = -iK|a|^2a + (G - \gamma|a|^2)a, \tag{2}$$

where K represents the Kerr nonlinearity. Substituting the general solution $a = A(t)e^{i\delta_f t}$ into Eq. (2), one obtains the frequency shift and amplitude:

$$\frac{dA}{dt} = (G - \gamma|A|^2)A, \quad \delta_f = -KA^2, \tag{3}$$

where A is the amplitude and δ_f denotes the resulting frequency shift. Hence, the vdP-D oscillator will reach stability at the same condition as the vdP oscillator $|A| = |a_0| = \sqrt{G/\gamma}$, while its frequency of the stable state is shifted to $\omega_s = \omega_1 - K|a_0|^2$, as shown in Fig. 1(c). Since the amplitude of the linear state is transient and small, this state is often overlooked. When researchers focus on the final amplitude, the modification given by the vdP-D oscillator can be considered negligible.

This idea is challenged in the coupled system. The interplay of gain and loss modes is highly discussed in acoustics [29,30], optomechanics [31], optics [32–35], spintronics [36,37], cavity magnonics [27,31,38,39], and microwave-power-transfer networks [40–42]. Here, we theoretically analyze a coherently coupled circuit as in the middle panel in Fig. 2(a). The damped oscillator ω_2 features an adjustable frequency and a constant loss factor κ. The coupling strength, caused by the inductor, is approximately set as a real-value constant J. If we assume that two oscillators share the same reference frequency $\omega_r = \frac{1}{2}[\omega_1 + \omega_2]$, $V_1(t) = \frac{1}{2}[a(t)e^{i\omega_r t} + \text{c.c.}]$, and $V_2(t) = \frac{1}{2}[m(t)e^{i\omega_r t} + \text{c.c.}]$, the dynamics of this coupled system can be written in the following form [43]:

$$\begin{pmatrix} \dot{a} \\ \dot{m} \end{pmatrix} = i \begin{pmatrix} -\frac{\Delta_{21}}{2} + \mathscr{F}(|a|) + J & -J \\ -J & \frac{\Delta_{21}}{2} + i\kappa + J \end{pmatrix} \begin{pmatrix} a \\ m \end{pmatrix}. \tag{4}$$

Here we define the theoretical notation $\Delta_{21} = \omega_2 - \omega_1$, which can be transformed to the effective detuning, $\omega_2 - \omega_s = \Delta_{21} + K|a_0|^2$. The function $\mathscr{F}$ is written as

$$\mathscr{F} = -K|a|^2 - i(G - \gamma|a|^2). \tag{5}$$

For $K = 0$, Eq. (4) refers to the coupling of the vdP oscillator and a damped oscillator as in the top panel in Fig. 2(a). In the case of $K \neq 0$, the equation describes the coupling of the vdP-D oscillator and a damped oscillator as in the bottom panel in Fig. 2(a).

The stable amplitude of the coupled system, $|a| = |a_c|$, is determined when the eigenvalues are purely real, indicating a balanced state of gain and loss. Given this stable-state condition, the eigenfrequency can be derived from the

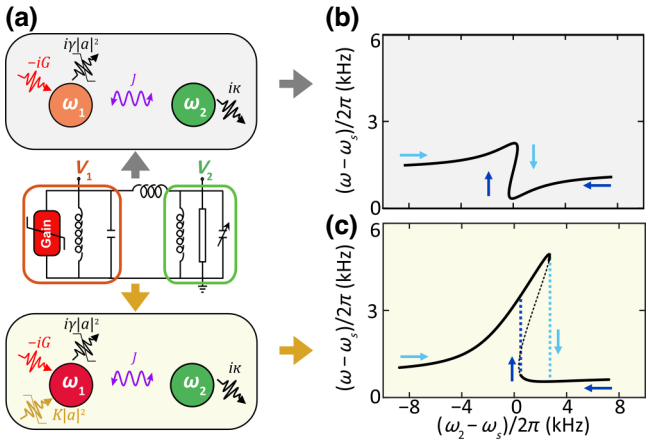

FIG. 2. (a) Two coupling diagrams for coherently coupled *LRC* circuits. (b),(c) Calculated coupled frequency for the two diagrams, where $\kappa/2\pi = 0.87$ kHz and $J/2\pi = 1.29$ kHz.

following equations:

$$\omega(|a_c|)_\pm = \mathscr{C} \pm \sqrt{(\Delta_{21} + i\kappa - \mathscr{F})^2/4 + J^2},$$
$$\mathrm{Im}[\omega(|a_c|)_\pm] = 0, \tag{6}$$

where $\mathscr{C} = (\mathscr{F} + i\kappa)/2 + J$. The corresponding stable eigenvectors are also obtained:

$$|\omega_\pm\rangle = \begin{pmatrix} 1 \\ \left.\frac{m}{a}\right|_\pm \end{pmatrix} = \begin{pmatrix} 1 \\ \frac{-\frac{\Delta_{21}}{2} + \mathscr{F} + J - \omega_\pm}{J} \end{pmatrix}. \tag{7}$$

The solved eigenfrequencies are depicted in Figs. 2(b) and 2(c), where the solid black lines represent the calculated stable eigenfrequencies and the dashed blue lines denote the transition between two eigenfrequency branches. The unstable solution, allowing $\omega_- > \omega_s + J$ or $\omega_+ < \omega_1 + J$, is denoted by dashed black lines.

Two distinctions arise between the system with the vdP oscillator and the system with the vdP-D oscillator. The first feature is that both singularities of the vdP-D oscillator shift away from zero detuning, while the vdP oscillator allows a transition around zero detuning. The other feature is strong bistability. Theoretical analysis suggests the coupling of a vdP oscillator might result in a narrow region exhibiting more than one eigenfrequency around zero detuning. However, the coupling of a vdP-D oscillator predicts that two distinct eigenfrequencies coexist across a broad range between the two dashed blue lines. This suggests that for the coupled system with the vdP-D oscillator, slow variation of the detuning $(\omega_2 - \omega_s)$ in two directions, as indicated by light-blue and dark-blue arrows, leads to distinct frequency dispersions and singularities. This behavior, where the system's state relies on the initial conditions, is referred to as "bistability."

III. CIRCUIT EXPERIMENT

On the basis of our theoretical model, we established an experimental setup as in Fig. 3(a) [43]. Oscillator 1 is an *LC* circuit integrated with a gain block consisting of an operational amplifier and a series of resistors. This module is powered by a voltage source V_{CC} [43]. We can control the gain as being ON or OFF by the voltage source. Oscillator 2 is a damped *LRC* circuit with adjustable frequency, achieved through a variable capacitor. The two oscillators are interconnected via an inductor and a large parallel resistance. This interconnection leads to a coupling factor, approximated as the complex constant $J/2\pi = (1.29 + i0.06)$ kHz. An oscilloscope is used to record the voltages at the nodes V_1 and V_2 of both *LRC* circuits.

With the switch turned off and the voltage source V_{CC} activated, we used the oscilloscope to capture the complete envelope of oscillator 1, ranging from minimal to stable amplitude. As depicted in Fig. 3(b), the voltage trigger of the oscilloscope was set at 1.1 V, enabling the oscilloscope to document voltages around this trigger. We divided the oscillation into three distinct time periods and performed a Fourier transform on each segment. The resulting spectra are shown in Fig. 3(c). A noticeable frequency shift is observed between the low-amplitude peak

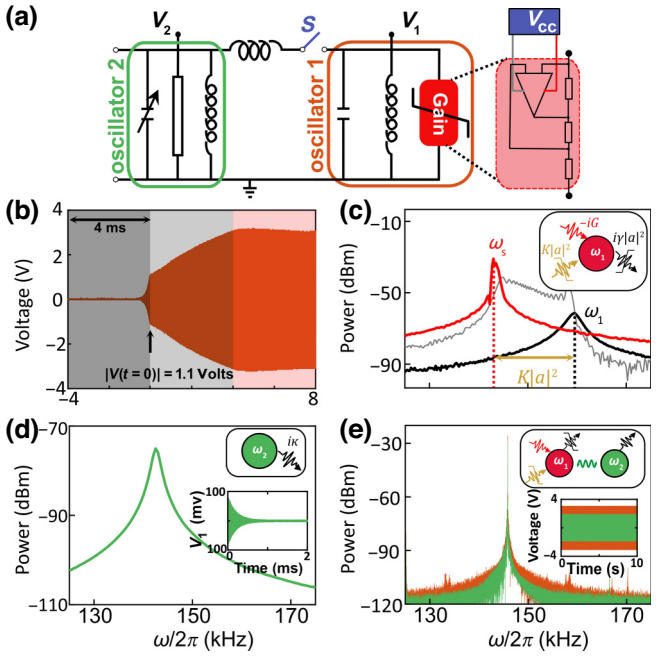

FIG. 3. (a) Experimental setup. (b) Complete voltage oscillation profile of an uncoupled gain-embedded circuit. (c) Spectral analysis over three distinct time intervals. (d) Spectrum of a damped *LRC* circuit, where the inset depicts the raw time-domain data. (e) By closure of the switch *S* to measure the stable coupled state, the spectrum is obtained from the time-domain oscillation in the inset.

at $\omega_1/2\pi = 159.40$ kHz, indicating the linear state, and the high-amplitude peak at $\omega_s/2\pi = 143.48$ kHz, indicating the stable state. The transition process is characterized by a broadened spectrum bridging these two states. From the time-domain oscillation, we determined the amplitude as $|a_0| = 3.16$ V, leading to a Kerr nonlinearity $K/2\pi = 1.59\,\text{kHz/V}^2$. The spectra demonstrate this gain-embedded oscillator has the feature of a vdP-D oscillator.

We used the oscilloscope to record the relaxation process of oscillator 2 and coupled stable states. The spectra of a single oscillator 2, transformed from its time-domain voltage oscillation, are presented in Fig. 3(d). This damped mode has a constant loss factor $\kappa/2\pi = 0.87$ kHz. On coupling of oscillator 2 with oscillator 1, shown in Fig. 3(e), despite the oscillation amplitudes differing within the two circuits, their spectra converge to the same peak. This indicates that the system manifests a degenerate eigenfrequency. By toggling the switch on and off, we can strictly calibrate uncoupled oscillations, and analyze the coupled oscillations.

Adjusting the variable capacitor, we systematically investigated the coupled properties dependent on detuning. For each detuning, the gain was activated and the system was measured for a stable amplitude; subsequently, the gain was turned off before we proceeded to the next detuning. Our measurement incorporated two distinct settings, determined by the sequence of powering the voltage source V_{CC} and engaging the coupling switch S, labeled as "S-V" and "V-S." In the "S-V" setting, where the voltage source V_{CC} is activated after closure of the switch S, the system begins its evolution from the coupling of linear state ω_1 and damped state ω_2. So the system is expected to start from a coupled state characterized by a small amplitude and negative detuning $\omega_2 - \omega_1 < 0$. In the "V-S" setting, where the voltage source V_{CC} is powered on before the switch S is closed, the system begins its evolution from the coupling of stable state ω_s and damped state ω_2. In this situation, the system is expected to start from $|a_0|$ of oscillator 1.

We measured amplitude, frequency, amplitude ratio, and relative phase of stable coupled states, under both the "S-V" setting and the "V-S" setting. Theoretical calculations were performed with fitted gain factor $G/2\pi = 7.74$ kHz, based on Eqs. (6) and (7). As shown in Fig. 4(a), in the "S-V" setting, the amplitude tends to select a small amplitude, while in the "V-S" setting, the amplitude tends to select the solutions close to $|a_0|$ of oscillator 1. The coupled state strongly depends on the initial conditions, showcasing the shifted singularities. Because of the strong bistability of the amplitude, we can also observe the bistable behavior of the frequency, amplitude ratio, and relative phase in Figs. 4(b)–4(d). The experimental results align well with the theoretical predictions.

This circuit experiment revealed unexpected results regarding the amplitude ratio. The coupled circuit, which is a standard model for innovative wireless-power-transfer

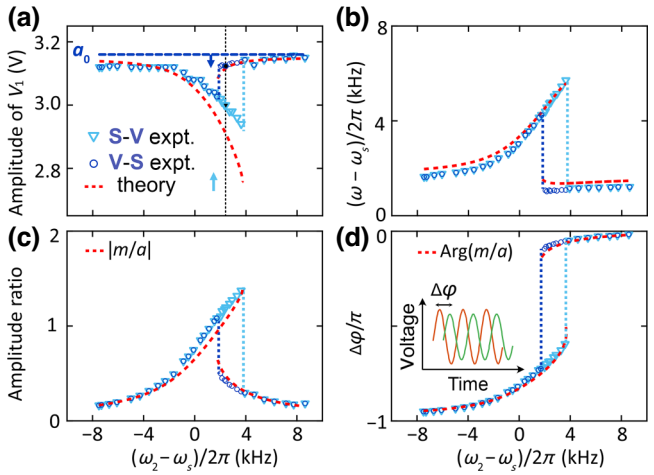

FIG. 4. Measurement of the gain-driven coupled system in "S-V" and "V-S" settings. (a) Relationship between detuning and the measured amplitude of V_1. (b) Dependence of the frequency on detuning. (c) Correlation between detuning and the amplitude ratio, denoted as $|m/a|$. (d) Dependence of the signals' relative phase $\Delta\varphi$ on detuning.

(WPT) technology, facilitates energy transmission from a gain-embedded oscillator to a damped oscillator, functioning, respectively, as the power source and receiver. Notably, our coupled circuit, based on the vdP-D oscillator, shows an amplitude ratio, as depicted in Fig. 4(c), that surpasses the unity value reported for the usual WPT model based on the vdP oscillator [40].

IV. CAVITY-MAGNONIC EXPERIMENT

The cavity-magnonic system comprises a gain-embedded open cavity and a YIG sphere, allowing the interaction between the cavity mode and the magnon mode. It is observed that the polariton's frequency dispersion depends on the initial conditions. In previous work, this system was phenomenologically understood as the coupling of a vdP oscillator and a damped oscillator, while the reliance on the initial conditions was attributed to dissipative coupling [27].

Our experiment demonstrated that the cavity mode is a vdP-D oscillator. As illustrated in Fig. 5(a), we engineered a gain-embedded half-wavelength transmission-line resonator, following the design specifications of Yao *et al.* [27]. The gain was implemented with use of a bipolar junction transistor, powered by voltage sources indicated as V_{BJT} [43]. Using a high-performance oscilloscope to capture the microwave signal, we observed the complete signal envelope as shown in Fig. 5(b). The complete signal is presented in segment form to better show the signal-amplitude growth for t_1.

Applying the Fourier transform to the data collected during four time periods t_1–t_4, we acquired the corresponding spectral evolution as shown in Fig. 5(c).

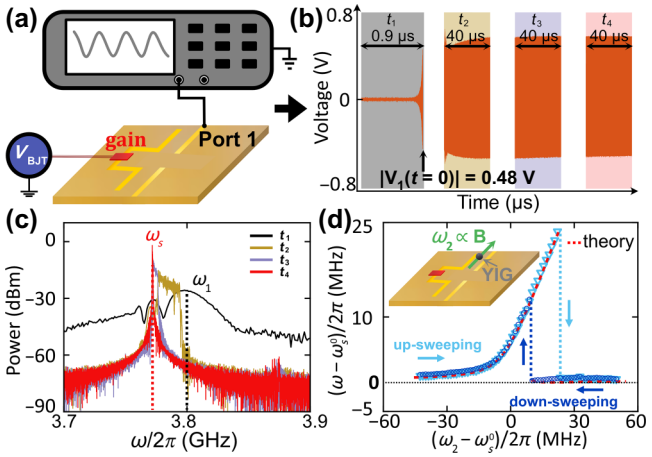

FIG. 5. (a) Experimental setup of a gain-embedded cavity, comprising an embedded gain element and a transmission-line resonator. (b) Complete voltage oscillation profile of the cavity measured by the oscilloscope, where the voltage trigger is set as 0.48 V. (c) Spectrum over four intervals of the segmented time-domain dynamics. (d) By coupling of the YIG sphere with the gain-embedded cavity, bistability is observed by different sweeping settings.

Echoing Fig. 3(c), the spectrum progressively transitions from a low-amplitude profile at $\omega_1/2\pi = 3.801$ GHz to a sharp, high-amplitude frequency peak at $\omega_s/2\pi = 3.772$ GHz. Given the time-domain oscillation for t_4, the amplitude is obtained as $|a_0| = 0.55$ V, leading to $K/2\pi = 95.936$ MHz/V^2. Notably, the t_1 spectrum indicates that the initial small-amplitude oscillation in the gain-embedded cavity, unlike that in the circuit, does not align with a simple linear mode. However, the spectra for t_2, t_3, and t_4 confirm the occurrence of frequency shifting within this cavity mode.

Figure 5(d) shows the observed frequency dispersion. The inset shows a schematic of the experimental setup. A YIG sphere is positioned within the gap of the transmission lines, above the cavity plane. The frequency of the magnon mode is linearly dependent on the magnetic field, denoted as $\omega_2 \propto B$, allowing an adjustable frequency range between 3.720 and 3.840 GHz. The loss factor of the magnon mode is calibrated as a constant $\kappa/2\pi = 2.477$ MHz.

By our continuously changing the magnetic field, the frequency dispersion is measured. The degenerate frequency for each detuning is obtained from the Fourier transform, where the frequency of the largest detuning is set as a reference $\omega_s^0/2\pi$. The coupling factor is defined as a purely real value as detailed in Supplemental Material [43] (where Refs. [27,28,44–46] are cited), $J/2\pi = 3.890$ MHz. Given a fitting gain factor $G/2\pi = 6.397$ MHz, the coupling theory based on the vdP-D oscillator aligns with the experimental results. As we anticipated in the theory, by our slowly sweeping the detuning, the two settings, up-sweeping and down-sweeping, result in two frequency-dispersion traces. The up-sweeping setting yields a singularity appearing further away from the zero-detuning point than for the down-sweeping setting.

V. CONCLUSION

Our study elucidates the coupling physics of the vdP-D oscillator under conditions of weak nonlinearity. By incorporation of the Duffing term, the vdP-D oscillator can operate across a broader frequency dynamic range, enabling a more-extensive dispersive coupling in the coupled system. This coupling theory was validated through circuit experiments. It was found that oscillations generated by the vdP-D circuit can induce a more-intense amplitude response in the damped circuit than traditionally expected from the standard vdP circuit used in WPT technology.

We demonstrated that a gain-embedded microwave cavity can be effectively modeled as a vdP-D oscillator. The wide frequency dynamic range of the vdP-D cavity provides an alternative perspective on the behavior of gain-driven polaritons and their bistability. Unlike the traveling-wave model, which depends on an open system to influence oscillator interactions, our model uses the inherent Kerr nonlinearity of the cavity itself. This approach simplifies the realization of gain-driven polaritons, emphasizing the vdP-D oscillator's importance in coupled systems. Given the prevalence of Duffing and Kerr nonlinearity in various systems, including microwave systems, optical fibers, and magnetic materials, our findings might attract broad interest in the field of non-Hermitian coupling physics.

ACKNOWLEDGMENTS

This work was funded by NSERC Discovery Grants, NSERC Discovery Accelerator Supplements, Innovation Proof-of Concept Grant of Research Manitoba, and Faculty of Science Research Innovation and Commercialization Grant of University of Manitoba (C.-M.H.). C.Z. is supported by the China Scholarship Council (Grant No. CSC202106180012).

[1] B. van der Pol and J. van Der Mark, Frequency demultiplication, Nature **120**, 363 (1927).
[2] S. H. Strogatz, *Nonlinear Dynamics and Chaos: With Applications to Physics, Biology, Chemistry, and Engineering (Second Edition)* (CRC Press, Boca Raton, 2015), p. 200.
[3] T. Matsumoto, Chaos in electronic circuits, Proc. IEEE **75**, 1033 (1987).
[4] I. S. Murray, *Laser Physics* (CRC Press, Boca Raton, 2018), p. 45.

[5] T. E. Lee and H. R. Sadeghpour, Quantum synchronization of quantum van der Pol oscillators with trapped ions, Phys. Rev. Lett. **111**, 234101 (2013).

[6] C. W. Wächtler and G. Platero, Topological synchronization of quantum van der Pol oscillators, Phys. Rev. Res. **5**, 023021 (2023).

[7] B. van der Pol and J. van der Mark, LXXII. The heartbeat considered as a relaxation oscillation, and an electrical model of the heart, Philos. Mag. **6**, 763 (1928).

[8] R. FitzHugh, Impulses and physiological states in theoretical models of nerve membrane, Biophys. J. **1**, 445 (1961).

[9] J. Aschoff, Circadian rhythms in man: A self-sustained oscillator with an inherent frequency underlies human 24-hour periodicity, Science **148**, 1427 (1965).

[10] R. Kitney, An analysis of the nonlinear behaviour of the human thermal vasomotor control system, J. Theor. Biol. **52**, 231 (1975).

[11] L. D. Landau and E. M. Lifshitz, *Mechanics* (CUP Archive, London, 1960), Vol. 1, p. 84.

[12] J. Kerr, XL. A new relation between electricity and light: Dielectrified media birefringent, London Edinburgh Philos. Mag. J. Sci. **50**, 337 (1875).

[13] G. P. Agrawal, *Nonlinear Fiber Optics (Third Edition)* (Academic Press, San Diego, 2001), p. 211.

[14] Y.-P. Wang, G.-Q. Zhang, D. Zhang, X.-Q. Luo, W. Xiong, S.-P. Wang, T.-F. Li, C.-M. Hu, and J. Q. You, Magnon Kerr effect in a strongly coupled cavity-magnon system, Phys. Rev. B **94**, 224410 (2016).

[15] Y.-P. Wang, G.-Q. Zhang, D. Zhang, T.-F. Li, C.-M. Hu, and J. Q. You, Bistability of cavity magnon polaritons, Phys. Rev. Lett. **120**, 057202 (2018).

[16] M. Shinriki, M. Yamamoto, and S. Mori, Multimode oscillations in a modified van der Pol oscillator containing a positive nonlinear conductance, Proc. IEEE **69**, 394 (1981).

[17] K. Murali and M. Lakshmanan, Transmission of signals by synchronization in a chaotic van der Pol–Duffing oscillator, Phys. Rev. E **48**, R1624 (1993).

[18] J. Xu and K. Chung, Effects of time delayed position feedback on a van der Pol–Duffing oscillator, Physica D **180**, 17 (2003).

[19] Z. Jing, Z. Yang, and T. Jiang, Complex dynamics in Duffing–van der Pol equation, Chaos Solitons Fractals **27**, 722 (2006).

[20] A. Kimiaeifar, A. Saidi, G. Bagheri, M. Rahimpour, and D. Domairry, Analytical solution for van der Pol–Duffing oscillators, Chaos Solitons Fractals **42**, 2660 (2009).

[21] Z. Zhihong and Y. Shaopu, Application of van der Pol–Duffing oscillator in weak signal detection, Comput. Electr. Eng. **41**, 1 (2015).

[22] H. Huebl, C. W. Zollitsch, J. Lotze, F. Hocke, M. Greifenstein, A. Marx, R. Gross, and S. T. B. Goennenwein, High cooperativity in coupled microwave resonator ferrimagnetic insulator hybrids, Phys. Rev. Lett. **111**, 127003 (2013).

[23] Y. Tabuchi, S. Ishino, T. Ishikawa, R. Yamazaki, K. Usami, and Y. Nakamura, Hybridizing ferromagnetic magnons and microwave photons in the quantum limit, Phys. Rev. Lett. **113**, 083603 (2014).

[24] X. Zhang, C.-L. Zou, L. Jiang, and H. X. Tang, Strongly coupled magnons and cavity microwave photons, Phys. Rev. Lett. **113**, 156401 (2014).

[25] M. Goryachev, W. G. Farr, D. L. Creedon, Y. Fan, M. Kostylev, and M. E. Tobar, High-cooperativity cavity QED with magnons at microwave frequencies, Phys. Rev. Appl. **2**, 054002 (2014).

[26] L. Bai, M. Harder, Y. P. Chen, X. Fan, J. Q. Xiao, and C.-M. Hu, Spin pumping in electrodynamically coupled magnon-photon systems, Phys. Rev. Lett. **114**, 227201 (2015).

[27] B. Yao, Y. S. Gui, J. W. Rao, Y. H. Zhang, W. Lu, and C.-M. Hu, Coherent microwave emission of gain-driven polaritons, Phys. Rev. Lett. **130**, 146702 (2023).

[28] D. M. Pozar, *Microwave Engineering* (John Wiley & Sons, Hoboken, 2011), p. 272.

[29] H. Jing, S. K. Özdemir, X.-Y. Lü, J. Zhang, L. Yang, and F. Nori, $\mathcal{PT}$-symmetric phonon laser, Phys. Rev. Lett. **113**, 053604 (2014).

[30] R. Fleury, D. Sounas, and A. Alù, An invisible acoustic sensor based on parity-time symmetry, Nat. Commun. **6**, 5905 (2015).

[31] X.-Y. Lü, H. Jing, J.-Y. Ma, and Y. Wu, $\mathcal{PT}$-symmetry-breaking chaos in optomechanics, Phys. Rev. Lett. **114**, 253601 (2015).

[32] H. Hodaei, M.-A. Miri, M. Heinrich, D. N. Christodoulides, and M. Khajavikhan, Parity-time–symmetric microring lasers, Science **346**, 975 (2014).

[33] Y. Liu, T. Hao, W. Li, J. Capmany, N. Zhu, and M. Li, Observation of parity-time symmetry in microwave photonics, Light Sci. Appl. **7**, 38 (2018).

[34] Ş. K. Özdemir, S. Rotter, F. Nori, and L. Yang, Parity–time symmetry and exceptional points in photonics, Nat. Mater. **18**, 783 (2019).

[35] J. Zhang, L. Li, G. Wang, X. Feng, B.-O. Guan, and J. Yao, Parity-time symmetry in wavelength space within a single spatial resonator, Nat. Commun. **11**, 3217 (2020).

[36] J. M. Lee, T. Kottos, and B. Shapiro, Macroscopic magnetic structures with balanced gain and loss, Phys. Rev. B **91**, 094416 (2015).

[37] A. Galda and V. M. Vinokur, Parity-time symmetry breaking in magnetic systems, Phys. Rev. B **94**, 020408(R) (2016).

[38] Y. Cao and P. Yan, Exceptional magnetic sensitivity of $\mathcal{PT}$-symmetric cavity magnon polaritons, Phys. Rev. B **99**, 214415 (2019).

[39] M. Kim, C. Zhang, C. Lu, and C.-M. Hu, Low phase noise microwave oscillator based on gain driven polariton, Appl. Phys. Lett. **124**, 114103 (2024).

[40] S. Assawaworrarit, X. Yu, and S. Fan, Robust wireless power transfer using a nonlinear parity–time-symmetric circuit, Nature **546**, 387 (2017).

[41] S. Assawaworrarit and S. Fan, Robust and efficient wireless power transfer using a switch-mode implementation of a nonlinear parity–time symmetric circuit, Nat. Electron. **3**, 273 (2020).

[42] X. Hao, K. Yin, J. Zou, R. Wang, Y. Huang, X. Ma, and T. Dong, Frequency-stable robust wireless power transfer based on high-order pseudo-Hermitian physics, Phys. Rev. Lett. **130**, 077202 (2023).

[43] See Supplemental Material at http://link.aps.org/supplemental/10.1103/PhysRevApplied.22.014034 for the detailed setup and calibrations of experiments.

[44] I. Texas Instruments, NE5532x, SA5532x dual low-noise operational amplifiers (2015), https://www.ti.com/lit/gpn/ne5532.

[45] C. Kittel, On the theory of ferromagnetic resonance absorption, Phys. Rev. **73**, 155 (1948).

[46] M. Kim, Y. Yang, Y. S. Gui, and C.-M. Hu, Visualization of synchronization zone on the Bloch sphere through an anti-PT-symmetric electrical circuit, AIP Adv. **12**, 035217 (2022).